CoS$_2$ nanodots anchored into heteroatom-doped carbon layer via a biomimetic strategy: Boosting the oxygen evolution and supercapacitor performance

Bingyue Li [a], Ruimin Xing [a,*], Santosh V. Mohite [a], Sanjay S. Latthe [a], Akira Fujishima [b], Shanhu Liu [a,**], Yanmei Zhou [a]

[a] Henan Key Laboratory of Polyoxometalate Chemistry, Henan Joint International Research Laboratory of environmental pollution control materials, College of Chemistry and Chemical Engineering, Henan University, Kaifeng, 47504, PR China
[b] Research Institute for Science and Technology, Photocatalysis International Research Center, Tokyo University of Science, 2641 Yamazaki, Noda, Chiba, 278-8510, Japan

HIGHLIGHTS

- A biomimetic strategy was developed to anchor CoS$_2$ into heteroatom-doped carbon.
- Numerous CoS$_2$ nanodots and heteroatom dopants offered abundant active sites.
- An attractive OER overpotential of 226 mv at 10 mA cm^{-2} was obtained.
- Nearly ~100% capability retention after 10000 cycles was achieved.
- The rational design concept can be extended to other metal sulfides/carbon hybrids.

GRAPHICAL ABSTRACT
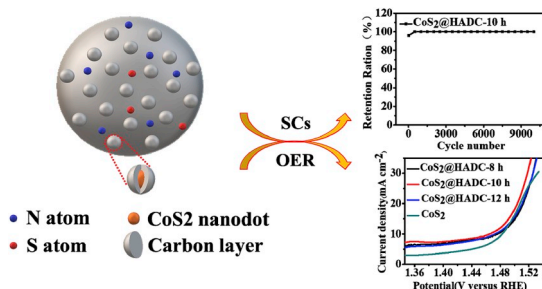
ABSTRACT

Development of efficient and durable electrocatalysts and electrode materials are significantly important to enhance the electrochemical performance for oxygen evolution reaction and supercapacitor applications. Herein, we design a hydrothermal-assisted biomimetic strategy to anchor CoS$_2$ nanodots on heteroatom-doped carbon layer (CoS$_2$@HADC). Numerous CoS$_2$ nanodots and heteroatoms rich in N and S are *in situ* hybridized into the carbon layer in a homogeneously dispersed manner. The preparation procedure is quite simple and moderate, avoiding the high-temperature annealing step. The optimized hybrid not only act as effective electrocatalyst, in which overpotential of 226 mv is enough to drive a current density of 10 mA cm^{-2} with a Tafel slope of 56 mV Dec^{-1} during the OER process, but also serve as electrode material with specific capacitance of 565 F g^{-1} at a current density of 1 A g^{-1} for high-performance supercapacitor, compared with CoS$_2$ (176 F g^{-1}). Also, it exhibits superior cycling activity (~100% capability retention after 10000 cycles at 2 A g^{-1} in 6.0 M KOH) and remains a 57% high rate capability (320 F g^{-1} at 5 A g^{-1}). The rational design concept for cobalt sulfides/heteroatom-doped carbon hybrid provide a simple strategy towards superior energy conversion and storage devices.

* Corresponding author.
** Corresponding author.
  E-mail addresses: xingenjoy@163.com (R. Xing), liushanhu@vip.henu.edu.cn (S. Liu).

1. Introduction

With increasingly global population growth and serious environmental problems, great concern has been paid to the next-generation technologies towards effective energy storage and clean energy conversion devices [1,2]. Among them, hydrogen production via electrochemical water splitting becomes highly appealing because of the abundant presence of water for clean energy. But the anodic water electrolysis reaction, that is oxygen evolution reaction (OER), is kinetically sluggish and generally demands a considerable overpotential to drive the required current densities above $10\,mA\,cm^{-2}$. Besides of the noble metal catalysts, first-row transition metal-based oxides/sulfides often outperform in terms of OER activity [3,4]. In particular, cobalt sulfides with different phases such as CoS_2, Co_3S_4, and Co_9S_8 became the focus as highly active electrocatalysts with the merit of superior electrical conductivity, which provide short path lengths for transporting electrons [5]; but their low rate capability and poor cycling stability limit its feasible application for OER. Recently, electrochemical activities of cobalt sulfides are significantly enhanced by being involved with carbon-based materials [6–10]. The multi-component nanostructured hybrids offer improved stability and efficient rate capability that greatly contribute on the electrochemical performance [11].

Supercapacitors (SCs) integrated between high energy batteries and high power dielectric capacitors, have drawn great attention with the potential for extraordinary energy storage and durable charge/discharge lifecycle [12–14]. As a key component of SCs, electrode materials decided the whole electrochemical performance. So far, carbon materials are often used as commercial electrode materials due to the cheap, lightweight and fine features; but the limited charges physically stored on the carbon materials limited the practical applications of SCs. Therefore, to develop an alternative electrode material with higher specific capacitance is the current research hotspot. In particular, biocarbon enriched with multiple heteroatoms (such as N, S) could offer abundant active sites and gained more interest as electrode material, which have been prepared from some biomass, including human hair [15], leaves [16], soybean [17] and sepia [18]. However, the preparation processes commonly involved high-temperature pyrolysis carbonization and complicated strong base activation, which were time- and energy-consuming [19]. On the other hand, transition metal sulfides with high theoretical specific capacity are promising electroactive materials, but their low rate capability, poor cycling stability and electric conductivity also confined their further application in SCs. Therefore, another effective approach to improve the energy density and the cycling stability is to hybridize transition metal sulfides with carbon-based electrode layer. Furthermore, it is of great significance to develop a low-temperature solution-based route for the practical applications in these fields namely as OER [20] and supercapacitor [21].

Inspired by these findings, we designed a novel hybrid nanostructure CoS_2@HADC consisting of monodispersed crystalline CoS_2 nanodots anchored on protein-derived carbon layer decorating with *in situ* doped heteroatoms (e.g. N and S). Bovine serum albumin (BSA), a common commercially available protein, has been widely used to prepare various inorganic nanomaterials, including noble metal nanoclusters and transition metal sulfides [22,23]. However, BSA has hardly been used as scaffolds to provide heteroatom-doped carbon framework. Herein, BSA was selected as the model protein for the biomimetic confined synthesis of CoS_2 and expected to supply *in situ* heteroatom-doped carbon via the hydrothermal processes. The synthesis was a pioneering work achieved via a hydrothermal-assisted biomimetic procedure, which belongs to a solution-based method, avoiding the high-temperature annealing step usually required in the preparation of metal oxides. The facile low-temperature solution-based method not only ensured the formation of weak crystalline CoS_2 nanodots within a confined domain, but also sufficient heteroatoms (e.g. nitrogen and sulfur) were retained into carbon layer under the hydrothermal carbonization. Thus, the hybrid nanostructure provided abundant active sites and excellent hydrophilic

properties for aqueous electrolytes, boosting remarkable catalytic performances for OER and contributing a lot pseudo-capacitance for SCs in basic electrolyte.

2. Experimental section

2.1. Reagents and materials

Bovine serum albumin (BSA), cobalt (II) nitrate hexahydrate (Co (NO$_3$)$_2$·6H$_2$O), and thioacetamide (CH$_3$CSNH$_2$, TAA) were obtained from Toray Industries, Inc. Analytical grade reagents are used without further purification.

2.2. Synthesis of CoS$_2$@HADC hybrids

CoS$_2$@HADC were obtained via a hydrothermal-assisted biomimetic strategy. Typically, 10 mL of Co(NO$_3$)$_2$·6H$_2$O aqueous solution (20 mM) were added dropwise into 30 ml of BSA aqueous solution (20 mg/mL) under magnetic stirring. The mixed solution was kept being stirred for 6 h to achieve the coordination equilibrium between BSA and Co^{2+} ions. Afterwards, 10 mL of TAA aqueous solution (50 mM) was added dropwise into the above mixed solution to form a transparent homogeneous solution. Then, the solution was transferred into a 50 ml autoclave and held at 200 °C for 10 h. The product was cooled to room temperature, washed several times and dried, which was denoted as CoS$_2$@HADC-10 h-200 °C. For comparison, CoS$_2$@HADC-8 h and CoS$_2$@HADC-12 h were prepared under the similar procedure at 200 °C with different hydrothermal time.

2.3. Material characterization

Powder X-ray diffraction (XRD) data were obtained on an X-ray D8 Advance instrument (Bruker, Germany). Scanning electron microscopy (SEM) equipped with energy dispersive X-ray (EDX) measurements were carried on a JSM-7610F scanning electron microscope (Hitachi). Transmission electron microscopy (TEM) equipped with selected area electron diffraction (SAED) measurements were performed on a JEOL JEM-2100 transmission electron microscope. X-ray photoelectron spectroscopy (XPS) analysis was performed on a Thermo Scientific Escalab 250Xi equipped with 150 W monochromatized Al K$_\alpha$ radiation (hv = 1486.6 eV), where all peaks were referred to the signature C1s peak for adventitious carbon at 284.8 eV. Brunauer– Emmett–Teller (BET) specific surface areas were measured by using Autosorb-IQ-MP-C system (Quantachrome, USA).

2.4. Electrochemical measurement

Nickel foam substrates ($1 \times 1\,cm^2$) were coated with 0.4 mL of a homogeneous slurry containing 0.37 mL of ethanol, 0.03 mL of 5 wt% Nafion and 2 mg of the catalysts (CoS$_2$ or CoS$_2$@HADC-x), which were as electrodes materials for supercapacitor and also as electrocatalyst for OER.

All the electrochemical measurements were conducted at room temperature using CHI650D (Chenghua, Shanghai China) electrochemical work station. For OER, the three-electrode system was composed of a Hg/HgO reference electrode, a graphite counter electrode, and a working electrode coated with a catalyst-loaded nickel foam substrate. Linear sweep voltammograms (LSVs) was performed in 1.0 M KOH at a scan rate of $2\,mV\,s^{-1}$ with the potential range from 0.2 to 1.0 V. Unless specified otherwise, all the reported potentials were calibrated with reference to the reversible hydrogen electrode (RHE) based on the following equation:

$$E_{vs.}\,RHE = E_{vs.}\,SCE + 0.059 \times pH + 0.241 \text{ in } 1.0\,M\,KOH \tag{1}$$

The overpotential values were calculated by using the following

equations.

$$\eta(V) = E_{vs.\ RHE} - 1.23 \qquad (2)$$

Electrochemical impedance spectroscopy (EIS) measurements were carried out in the same configuration at 1.24 V vs. RHE in the frequency range of 0.1 Hz–100 kHz with an AC voltage of 10 mV.

For supercapacitor measurements, all tests were performed in a 6.0 M KOH electrolyte with the three-electrode system including a Ag/AgCl reference electrode, a platinum counter electrode, and a working electrode coated with a catalyst-loaded nickel foam substrate. Cyclic voltammetry (CV) measurements were performed between −1.1 and −0.2 V at various scan rates ranging from 5 to 100 mV s^{-1}. Galvanostatic charge-discharge (GCD) measurements were conducted within the range of −1.1 to −0.2 V at different current densities from 1 A g^{-1} to 10 A g^{-1}. The specific capacitance (C_s) of the electrodes was calculated from GCD curves using following equation:

$$C_s = (I \cdot t)/(\Delta V \cdot m) \qquad (3)$$

where, I (mA) is the constant discharge current, t (s) is the discharge time, ΔV (V) is the window potential upon discharging, and m (mg) is deposited mass of the active materials which is dipped in electrolyte solution.

3. Results and discussion

3.1. Structural and composition analysis

CoS$_2$@HADC was conveniently synthesized by a hydrothermal-assisted biomimetic procedure and the schematic illustration was presented in Fig. 1. BSA firstly coordinated and sequestered with cobalt ions. The entrapped cobalt ions progressively *in situ* mineralized into cobalt sulfide into the confined protein scaffolds with the help of TAA. Under further hydrothermal treatment, CoS$_2$ nucleus became mature surrounded by *in situ* carbon incorporation based on the partial carbonization of the protein. As a result, CoS$_2$ nanodots embedded in heteroatoms-doped carbon layer were obtained. Compared with the previous studies, the preparation procedure was quite simple and moderate with no high-temperature pyrolysis and carbonization required. For comparison, two control experiments were conducted; the BSA solution obtained under hydrothermal treatment (200 °C for 10 h) was still brown-yellow without precipices observed, indicating CoS$_2$@HADC underwent a metal-assisted carbonization process, while CoS$_2$ without BSA was also prepared under the same hydrothermal treatment as another control.

XRD patterns were investigated to supply the crystal structures of the hybrids. As Fig. 2. shows, the hybrids exhibited broadening XRD patterns and grew sharper with prolonging the hydrothermal time, while well-defined CoS$_2$ crystallites were obtained in the absence of BSA. All the XRD patterns matched with the standard cubic pyrite structure of CoS$_2$ (JCPDS file No. 41–1471), in which the diffractions peaks, weaker but still distinct, at 2Θ of 32.3°, 36.2°, and 54.9°, corresponded to the
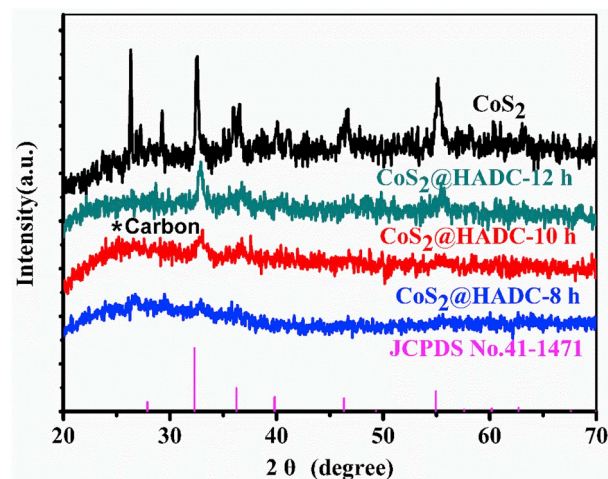

Fig. 2. XRD patterns of CoS$_2$ and CoS$_2$@HADC hybrids with different hydrothermal time.

Miller indices of (200), (210), (311) of CoS$_2$, respectively. Besides, a broad peak centered at 24° corresponded to the (002) reflection of carbon, indicating the amorphous feature of the carbon layer.

The morphology and microstructures of CoS$_2$@HADC-10 h-200 °C were investigated by using SEM. CoS$_2$@HADC-10 h-200 °C have an irregular aggregated morphology consisting of numerous particular nanoparticles (~20 nm). (Fig. 3a). The elemental distribution in the hybrid was evidenced by elemental mapping analysis (Fig. 3b), in which C, Co, S, N, and O distributed in a homogeneous manner throughout the hybrid. A typical TEM image (Fig. 3c) of the hybrid demonstrated that numerous nanodots (~2 nm) were homogeneously embedded into the amorphous carbon layer; these nanodots exhibited clear lattice fringes and the spacings is 0.2769 nm (Fig. 3d), in accord with the values for (200) planes of a cubic pyrite structure of CoS$_2$. The monodispersed crystallite CoS$_2$ nanodots and heteroatom dopants could offer abundant active sites and excellent wettability for contacting with the electrolyte and oxygen; also, these CoS$_2$ nanodots encapsulated into the protective carbon layers could avoid the detachment and aggregation from the carbon framework to survive long-term operation [24].

The presence of defect-rich graphitic carbon within CoS$_2$@HADC are further confirmed by Raman spectroscopy. As shown in Fig. 4, as for CoS$_2$@HADC-10 h-200 °C, the carbon layer exhibited G band and D band at around 1354 and 1581 cm^{-1}, respectively. G band can be used to explain the degree of carbon graphitization, while D band corresponded to partially disordered carbon with structural defects [25]. The band intensity ratio (I_D/I_G) is calculated 0.76. When varying the hydrothermal time, the I_D/I_G ratio dropped from 0.86 (CoS$_2$@HADC-8 h), 0.76 (CoS$_2$@HADC-10 h) to 0.48 (CoS$_2$@HADC-12 h), an indication of the decrease of defects in the carbon structure (Fig. S2) [26]. Furthermore, the two distinct bands (G band and D band) were not found in Raman
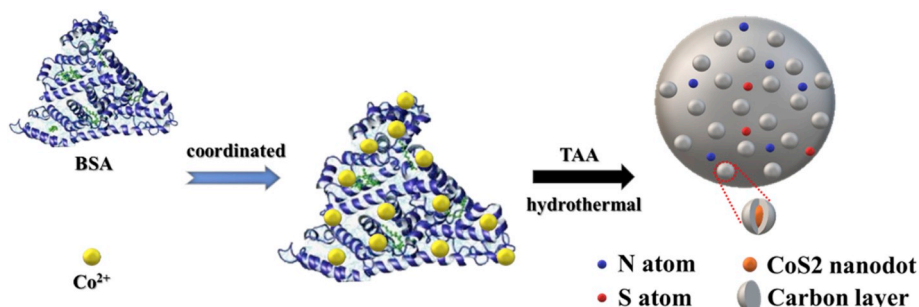

Fig. 1. Schematic illustration of the preparation processes of CoS$_2$@HADC composites.
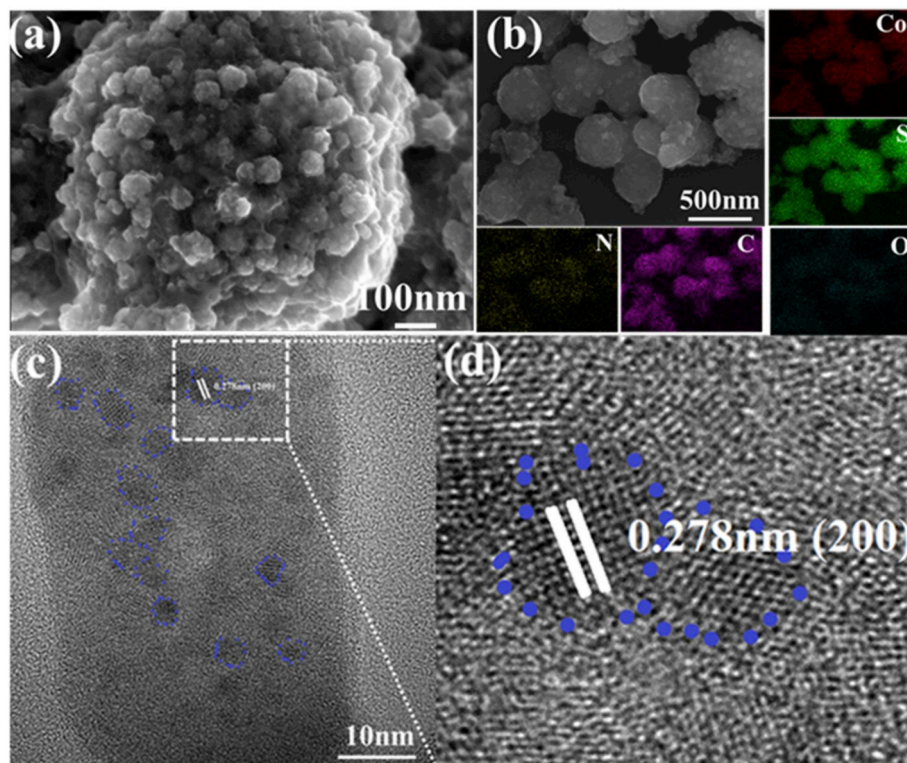
Fig. 3. SEM image (a), elemental mapping images (b), TEM image (c) and high-resolution TEM image (d) of CoS$_2$@HADC-10 h-200 °C.
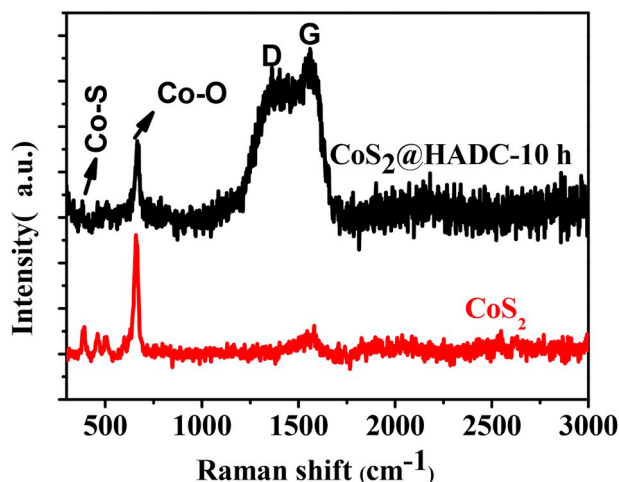

Fig. 4. Raman spectroscopy of CoS$_2$ and CoS$_2$@HADC-10 h-200 °C.

spectra of CoS$_2$ and CoS$_2$@HADC-10 h-220 °C (Fig. S3), indicating the absence of carbon materials. The latter could be explained given that the intramolecular disintegration of BSA and the collapse of the carbon framework at 220 °C, which could be confirmed based on the TG results (Fig. S4). In addition, a sharp peak at 658 cm^{-1} was assigned to be Co–O phase and a weak peak at 372 cm^{-1} was attributed to be Co–S phase [27]. For comparison, CoS$_2$ was easier to transform CoO without BSA protection. FT-IR spectra of CoS$_2$@HADC-10 h (Fig. S5) further confirmed that the stretching vibrations of Co–S bonds appeared at 550 cm^{-1} and bending vibrations of the sulfide groups appeared at 1103 cm^{-1} [28]; besides, the C=C skeletal vibrations at 1643 and 1514 cm^{-1} and the C=S stretching mode at 1140 cm^{-1} were also observed [29]. The above results demonstrated that proper hydrothermal temperature and time were important to ensure the partially

carbonization of the BSA protein and the nucleation and growth of CoS$_2$.

X-ray photoelectron spectroscopy (XPS) was used to analyze the elemental composition and heteroatom-doped configurations of CoS$_2$@HADC-10 h. As Fig. 5a shows, the typical survey spectra of CoS$_2$@HADC-10h-200 °C show all the presence of Co2p, O1s, N1s, C1s, and S2p at 778.4, 531.7, 399.92, 284.8 and 162.31 eV, with the corresponding atomic percent of 8.88%, 18.84%, 6.35%, 45.56% and 20.37%, respectively. The high content of C suggested the retention of the protein framework, while the S atomic percent (20.37%) was twice more than Co atomic percent (8.88%), indicating that there must be some extra sulfur atoms as dopants incorporated into the carbon layer. It is reported that there are 17 disulfide bonds and one free thiol in cysteine residues in every BSA molecule, which might not only attract Co^{2+} ions, but also supply extra sulfur atoms for *in situ* doping under hydrothermal treatment.

In the case of the deconvoluted spectrum of Co2p peak (Fig. 5b), the fitting analysis revealed the coexistence of Co^{2+} and Co^{3+}, in which the binding energies at ~793.7 eV and ~778.7 eV corresponded to Co^{3+} 2p$_{1/2}$ and 2p$_{3/2}$, and the binding energies at ~796.0 eV and ~780.4 eV are attributed to Co^{2+} 2p$_{1/2}$ and 2p$_{3/2}$, respectively; their satellite peaks appeared at 801.9 eV [30]. In addition, peak deconvolution of S2p (Fig. 5c) indicated that a sharp peak at 162.0 eV was assigned to polymeric S$_n^{2-}$ (38%) and a peak at 163.3 eV was assigned to the thiophene-S (-C-S-C-) groups (42%) [31]; In addition, a small peak at 168.46 eV was assigned to be S–O species (20%), resulted from surface air exposure [32]. The polymeric S$_n^{2-}$ was believed to be beneficial in anchoring CoS$_2$ on carbon surface. Furthermore, the S doped sites with lower electronegativity are easier to host O$_2$, advancing water splitting.

Besides that, Peak deconvolution of O1s (Fig. 5d) indicated that there are three peaks at 531.3, 531.7, and 532.8 eV, which were assigned to the C=O groups (O-1, 43%), the C–OH and/or C–O–C groups (O-2, 31%) and carboxylic groups (O-3, 26%), respectively. Among them, the high content of O-1 groups indicated the partial retention of C=O species in BSA, which were electrochemically active to improve the pseudocapacitance; the other two oxygenated groups could enhance the
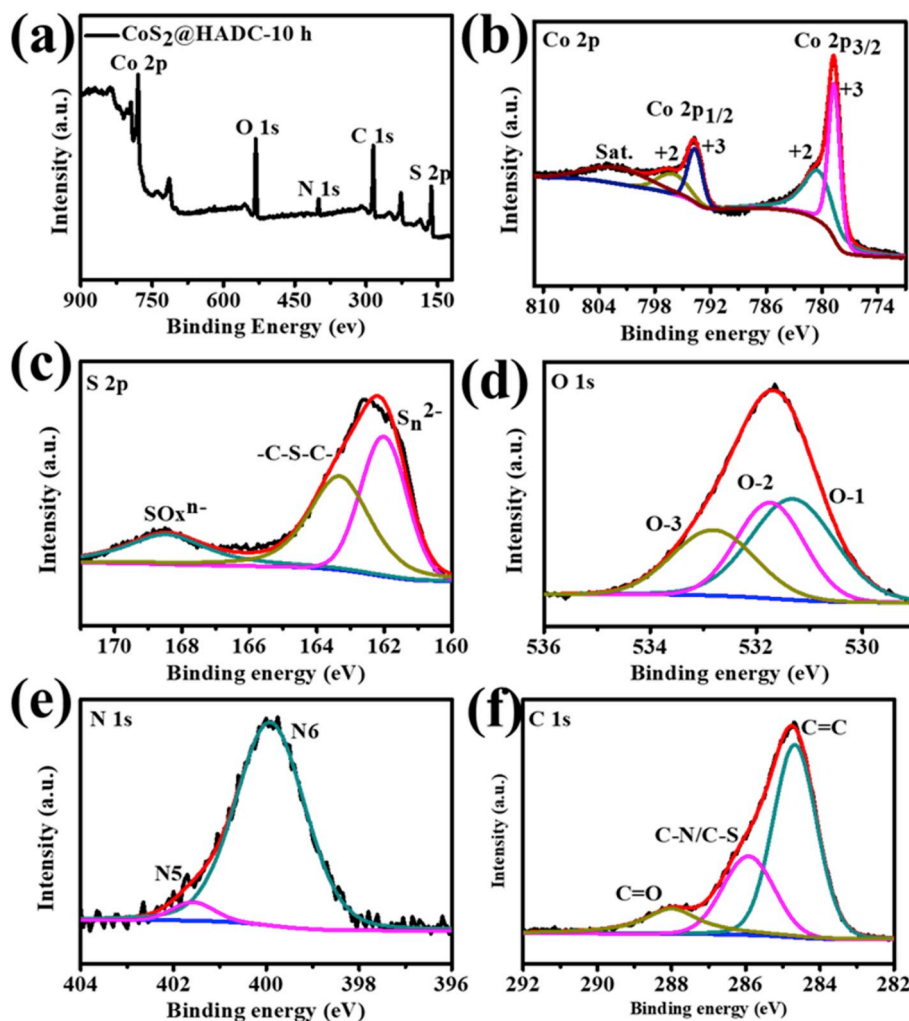
Fig. 5. XPS spectra of CoS$_2$@HADC-10 h. Survey scan (a), 2p core level of Co element (b), 2p core level of S of element (c), 1s core level of O element (d), 1s core level of N element (e) and 1s core level of C element (f).

wettability to aqueous electrolyte [33]. The N1s core level XPS spectrum (Fig. 5e) could be fitted into two peaks, consisting of pyridine-like N of 95% (N6 at 399.9 eV) and pyrrole-like N of 5% (N5 at 401.6 eV), which possess p-electrons to promote the π-conjugated system, thus improving the conductivity and pseudo-capacitances of the carbon layer [34]. It is reported that high-temperature pyrolysis is beneficial to graphitization in the presence of cobalt salt, resulting in the high content of graphitic N (401.2 eV). In our work, it is reasonable that graphitic N is absent under hydrothermal treatment at 200 °C. The high-resolution C1s XPS spectra (Fig. 5f) could be fitted into three peaks. A sharp main peak at 284.6 eV corresponded to carbon atoms (59%) from carbon framework, a peak at 285.9 eV suggested the C–N/C–S species (27%), indicating the successful *in situ* dopant of S and N into carbon layer, and another small peak at 288.0 eV was assigned to the C=O/C=N configuration (14%), indicating the partial retention of the carbon framework.

In conclusion, investigation by XPS proved the presence of CoS$_2$ and nitrogen- and sulfur-rich surface layer encapsulated into heteroatoms-doped carbon layer. Although the Brunauer Emmett-Teller (BET) surface area of CoS$_2$@HADC-10 h-200 °C obtained from the N$_2$ adsorption and desorption isotherms was about 17.076 m^2 g^{-1}(Fig. S6), which is lower than the most reported, numerous monodispersed nanodots and heteroatom dopants ensured more accessible active sites, thus rendering high electrical conductivity and superior electrocatalytic activity relative to CoS$_2$.

3.2. The OER activities

OER, as a half part of water splitting for energy conversion process, generally claim a considerable overpotential to drive the current density above 10 mA cm^{-2}. In this work, CoS$_2$@HADC were studied as electrocatalysts for OER of water electrolysis. The OER electrocatalytic performance were evaluated by using LSV technique at a scan rate of 2 mV s^{-1} in 1.0 M KOH solution. As Fig. 6a shows, compared to CoS$_2$, all of the hybrids CoS$_2$@HADC exhibited the improved OER activity. The optimized hybrid CoS$_2$@HADC-10 h-200 °C achieved the lowest overpotential of 226 mV at 10 mA/cm^2, compared with that of CoS$_2$ (256 mV), CoS$_2$@HADC-8 h (236 mV), CoS$_2$@HADC-12 h (236 mV), RuO$_2$ (320 mV). In addition, the OER performance of CoS$_2$@HADC-10 h is greatly superior to Co-based catalysts previously reported [35–37] (Table 1).

The OER kinetics were examined by the Tafel plots as shown in Fig. 6b. The Tafel slope of the optimized hybrid was 56 mV dec^{-1}, far below that of CoS$_2$ (93 mV dec^{-1}), CoS$_2$@HADC-8 h (75 mV dec^{-1}), and CoS$_2$@HADC-12 h (74 mV dec^{-1}). The electrochemical impedance spectra (EIS) of CoS$_2$ and CoS$_2$@HADC hybrids were conducted in a three-electrode configuration Fig. 6c. The solution resistance (Rs) is about 1.5 Ω and the CoS$_2$@HADC-10 h sample's Rct value is smaller than that of CoS$_2$, CoS$_2$@HADC-8 h, CoS$_2$@HADC-12 h. As we all know, the lower the Rct value, the more superior electrocatalytic activity the catalyst for HER and OER, the same trend as LSVs and Tafel slopes.
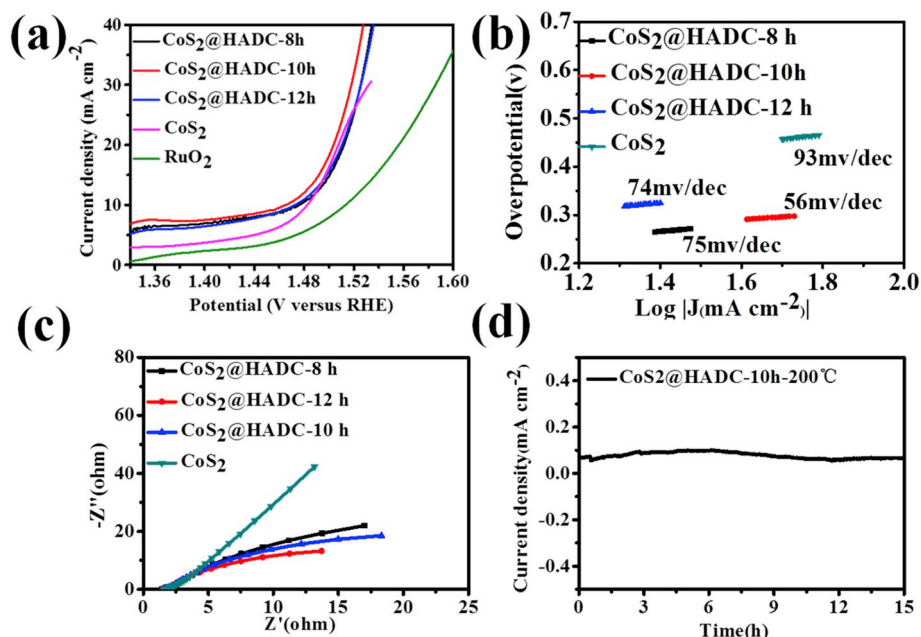
Fig. 6. Polarization curves (a), Tafel slope (b), and EIS (c) of CoS$_2$ and the hybrids CoS$_2$@HADC modified electrode in 1.0 M KOH, and stability test of CoS$_2$@HADC-10 h modified electrode (d).

Table 1
Comparison of OER activity data for Co-based non-noble metal catalysis.

Electrocatalyst	Substrate	Electrolyte	Overpotential @10 mA cm^{-2} (mV)	Tafel Slope (mV/Dec^1)	References
CoS$_2$@HADC	Nickel foam	1.0 M KOH	226	56.0	Present Work
CoS$_2$	–	0.1 M KOH	310	81.7	[29]
CoS$_2$/CC	Carbon cloth	1.0 M KOH	291	67.0	[30]
MOF CoS@CeOx	Glassy carbon	1.0 M KOH	269	50	[31]
CoS$_2$/CNT composites	Glassy carbon	0.1 M KOH	290	25.5	[6]
CoS$_2$/NSG	Glassy carbon	0.1 M KOH	393	81.0	[31]
Co$_9$S$_8$/NSG	Glassy carbon	1 M KOH	260	55	[38]

Therefore, it is concluded that the superior activity of CoS$_2$@HADC-10 h was benefited from the faster catalytic kinetics. For further studies, the OER stability measurement of the optimized hybrid was performed. Fig. 6d illustrates that the CoS$_2$@HADC-10 h retained steady OER activity and no noticeable potential augment was observed for more than 15 h of oxygen release. The overall structural features of the hybrid were kept but exhibited reduced structural order (Fig. S7). Elemental mapping analysis (Fig. S8) evidenced the drastic dropping of nitrogen and sulfur but the appearance of a great quantity of oxygen in the hybrid after the stability test. Besides, we compared the percentage contents of various chemical states of Co and S in CoS$_2$@HADC-10 h before and after the electrochemical test obtained by XPS and shown in Fig. S9 and Table 2. The deconvoluted spectra of Co 2p and S 2p showed that after

Table 2
The percentage contents of various chemical states of Co and S in CoS$_2$@HADC-10 h before and after the electrochemical test obtained by XPS.

	Electrochemical stability test of CoS$_2$@HADC-10 h	
Sample composition	before	after
Total Co (at. %)	8.88	7.03
Co^{3+}	52%	16%
Co^{2+}	48%	84%
Total S (at. %)	20.37	5.4
S$_n^{2-}$	38%	14%
C–S–C	42%	–
S–O	20%	86%

the electrochemical stability test, the percentage contents of Co^{3+}, S$_n^{2-}$ and C–S–C drastically dropped while the percentage contents of Co^{2+} and S–O drastically raised, which is a direct evidence of Co^{3+}, S$_n^{2-}$ and heteroatom dopants were active sites. Thus they are unstable in the OER process, and a superficial amorphous, (oxy)hydroxide layer (for example, CoO(OH) species) possibly formed through the dynamic surface self-reconstruction process [38,39].

3.3. Supercapacitor performance

The electrochemical performances of CoS$_2$ and CoS$_2$@HADC-10 h coated onto the nickel foam substrate were evaluated as electrode materials for SC performance. The GCD measurements of all samples (Fig. S10) were carried out at a current density of 1 A g^{-1} within a voltage ranging from −1.1 to −0.2 V. The CoS$_2$@HADC-10 h modified electrode shows the maximum discharge time as compared to the other electrodes. Cyclic voltammetry (CV) of CoS$_2$@HADC-10 h was illustrated in Fig. 7a. The curves presented rectangular features without apparent redox peaks appearing, suggesting high rate capability with a rapid ion transfer feature [40]. The GCD experiment was conducted to further study the capacitive performance. As Fig. 7b, as for the electrode modified with CoS$_2$@HADC-10 h, all the charge/discharge curves displayed a distorted triangle shape due to the presence of pseudo-capacitances. The specific capacitance is calculated to be 565, 431, 327, 320 and 233 F g^{-1} at the current density of 1, 2, 4, 5 and 10 A g^{-1}, respectively. The specific capacitance in this work is superior to the values of copper cobalt sulfide reported by Guo et al. (515 F g^{-1} at
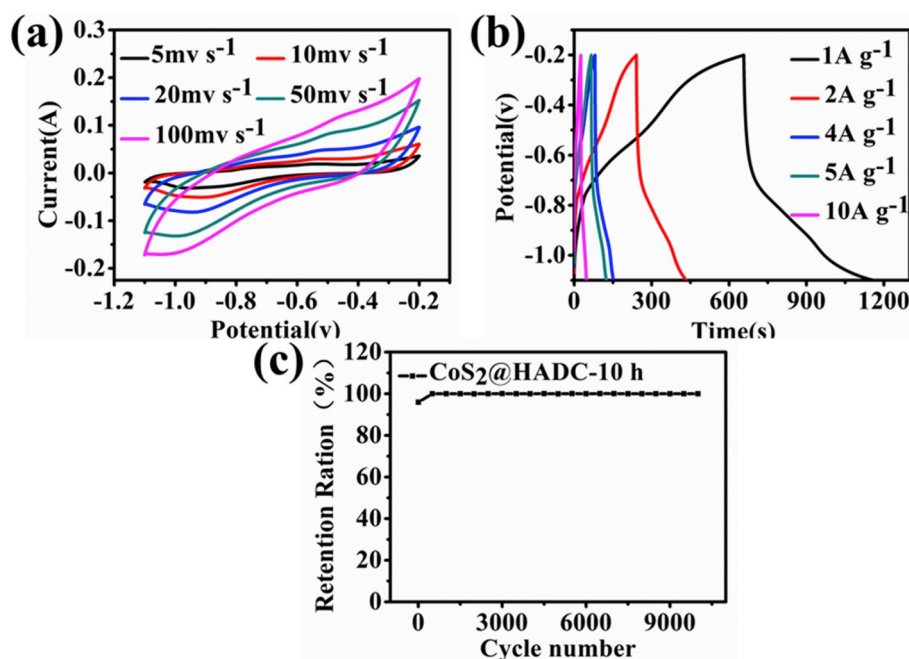
Fig. 7. CV curves (a) GCD curves (b) and cycling stability (c) of CoS_2@HADC-10 h.

$1 A g^{-1}$) and bifunctional cobalt sulfides reported by Ranaweera et al. ($420 F g^{-1}$ at $1 A g^{-1}$) [41,42]. Furthermore, the advantages such as higher current density, lower polarization and higher charge/discharge coulombic efficiency, are highly desirable for supercapacitor, which thus ensured the less time to finish a charge-discharge cycle. At lower current density, electrolyte ions could enter into the inner layer of electrode and fully contact with active material, thus resulting in a relatively bigger specific capacitance. On the contrary, at higher current density, only the outer surface of the electrode was exploited within the limited reaction time, thus resulting in a smaller specific capacitance. The long-term cycling stability of the studied supercapacitor was evaluated to examine the energy storage performance for potential applications. As shown in Fig. 7c, after 10000 charge/discharge cycles, the hybrid electrode almost kept the initial capacitance at a current density of $2 A g^{-1}$ the cycling stability of the hybrid electrode outshined the sulfide-based supercapacitors previously reported [43]. At the same time, we did more electrochemical test and and found the CoS_2@H-ADC-10 h had the best performance (Fig. S11). Monodispersed CoS_2 crystallite nanodots in refined form and heteroatom-doped carbon layer possibly provided a shorter ion diffusion path and lower charge-transfer resistance, thus resulting in the enhanced cycling ability [44].

4. Conclusions

In summary, we demonstrated a hybrid nanostructure composed of monodispersed CoS_2 nanodots anchored on heteroatom-doped carbon layer (CoS_2@HADC). The synthesis was achieved via a hydrothermal-assisted biomimetic procedure, avoiding the high-temperature annealing step usually required in the preparation of metal oxides. Weak crystalline CoS_2 nanodots within a confined domain and sufficient heteroatoms (e.g. sulfur and nitrogen) were *in situ* formed into carbon layers under the hydrothermal treatment. Thus, the hybrid nanostructure provided abundant active sites and excellent wettability for aqueous electrolytes. The optimized hybrid (CoS_2@HADC-10 h-200 °C) boosted remarkable catalytic performances for OER in basic electrolyte, with low Tafel slope (56 mV/Dec), small overpotential (226 mV at $10 mA cm^{-2}$), and nearly 100% Faradaic efficiencies. Moreover, the hybrid was a superior electrode material for high-performance SC, exhibiting high specific capacitance ($565 F g^{-1}$ at $1 A g^{-1}$) and superior cycling activity

(~100% capability retention after 10000 cycles at $2 A g^{-1}$). The reported method is universal and scalable for other transition metal sulfides and carbon substrates. Therefore, this biomimetic route is a pioneering strategy to design highly efficient next-generation electrocatalysts and electrode materials for OER and SC applications.

Conflicts of interest

There are no conflicts of interest to declare.

Acknowledgements

Appendix A. Supplementary data

Supplementary data to this article can be found online at https://doi.org/10.1016/j.jpowsour.2019.226862.

References

[1] M. Liu, Y. Pang, B. Zhang, L.P. De, O. Voznyy, J. Xu, X. Zheng, C.T. Dinh, F. Fan, C. Cao, Nat 537 (2016) 382.
[2] F. Song, L. Bai, A. Moysiadou, S. Lee, C. Hu, L. Liardet, X. Hu, J. Am. Chem. Soc. 140 (2018) 7748.
[3] T. Zhang, Y. Zhu, J.Y. Lee, J. Mater. Chem. A 6 (2018) 8147.
[4] Y. Luo, Z. Wang, Y. Fu, C. Jin, Q. Wei, R. Yang, J. Mater. Chem. A 4 (2016) 12583.
[5] X. Ma, W. Zhang, Y. Deng, C. Zhong, W. Hu, X. Han, Nanoscale 10 (2018) 4816.
[6] R. Nivetha, P. Kollu, K. Chandar, S. Pitchaimuthu, S.K. Jeong, A.N. Grace, RSC Adv. 9 (2019) 3215.
[7] J. Yang, Z. Yang, L. Li, Q. Cai, H. Nie, M. Ge, X. Chen, Y. Chen, S. Huang, Nanoscale 9 (2017) 6886.
[8] X. Zhang, L.X. Jie, G. Wang, H. Wang, J. Colloid Interface Sci. 505 (2017) 23.
[9] F. Han, C.Y.J. Tan, Z. Gao, J. Power Sources 339 (2017) 41.
[10] Y. Zhang, N. Wang, C. Sun, Z. Lu, X. Pan, B. Tang, Z. Bai, S. Dou, Y. Zhang, N. Wang, Chem. Eng. J. 332 (2018) 370.
[11] Y. Luo, C. Jin, Z. Wang, M. Wei, C. Yang, R. Yang, Y. Chen, M. Liu, J. Mater. Chem. A 5 (2017) 5690.
[12] F. Wang, X. Wu, X. Yuan, Z. Liu, Y. Zhang, L. Fu, Y. Zhu, Q. Zhou, Y. Wu, W. Huang, Chem. Soc. Rev. 46 (2017) 6816.

[13] D.P. Dubal, N.R. Chodankar, D.H. Kim, P. Gomezromero, Chem. Soc. Rev. 47 (2018) 2065.

[14] T. An, W. Cheng, J. Mater. Chem. A 6 (2018) 15478.

[15] W.J. Ma, N. Wang, Y.C. Du, P. Xu, B.J. Sun, L.J. Zhang, K.Y.A. Lin, ACS Sustain. Chem. Eng. 7 (2018) 2718.

[16] E. Hao, L. Wei, L. Shuang, Z. Yuan, H. Wang, S. Chen, F. Cheng, S. Zhao, H. Yang, J. Mater. Chem. A 5 (2016) 2204.

[17] C.A. Scaldaferri, V.M.D. Pasa, Fuel 245 (2019) 458.

[18] H.S. Kim, M. Kim, S.K. Min, J. Ahn, Y.E. Sung, W.C. Yoo, Acs Sust. Chem. Eng. 6 (2017) 2324.

[19] T. Asefa, X. Huang, Chem. Eur J. 23 (2017) 10703.

[20] Y. Hua, J. Hao, H. Jiang, H. Zhang, C. Li, Electrochim. Acta 278 (2018) 219.

[21] H. Wan, J. Xiao, J. Jiang, J. Yu, M. Ling, Z. Li, S. Bie, H. Chen, Y. Ruan, J. Power Sources 243 (2013) 396.

[22] S.N. Li, S. Zhao, R.M. Xing, V.S. Kumbhar, K. Lee, Y.M. Zhou, N. Kazuya, A. Fujishima, S.H. Liu, ChemNanoMat 5 (2019) 761.

[23] R. Xing, S. Liu, S. Tian, J. Nano Res. 13 (2011) 4847.

[24] D. Kong, C. Cheng, W. Ye, J.I. Wong, Y. Yang, H. Yang, J. Mater. Chem. A 3 (2015) 16150.

[25] Y. Tong, X. Yu, G. Shi, Phys. Chem. Chem. Phys. 19 (2017) 4821.

[26] L. Wang, S. Zhao, X. Wu, S. Guo, Z. Kang, RSC Adv. 6 (2016) 66893.

[27] M.M. Rahman, J. Ahmed, A.M. Asiri, I.A. Siddiquey, M.A. Hasnat, RSC Adv. 6 (2016) 90470.

[28] Y. Tang, C. Teng, S. Yu, Y. Qiao, S. Mu, S. Zhang, Y. Zhao, H. Li, W. Huang, F. Gao, J. Power Sources 295 (2015) 314.

[29] F. Luan, S. Zhang, D. Chen, K. Zheng, X. Zhuang, Talanta 182 (2018) 529.

[30] S.C. Huang, Y.Y. Meng, S.M. He, A. Goswami, Q.L. Wu, J.H. Li, S.F. Tong, T. Asefa, M.M. Wu, Adv. Funct. Mater. 27 (2017) 1.

[31] B.H. Chen, Z.Q. Jiang, L.S. Zhou, B.G. Deng, Z.J. Jiang, Z.L. Huang, M.L. Liu, J. Power Sources 389 (2018) 178.

[32] S. Shanmugam, P. Ganesan, M. Prabu, J. Sanetuntikul, ACS Catal. 5 (2015) 3625.

[33] H. Ma, C. Li, Z. Miao, J.D. Hong, G. Shi, J. Mater. Chem. A 5 (2017) 17040.

[34] Z.H. Sheng, L. Shao, J.J. Chen, W.J. Bao, F.B. Wang, X.H. Xia, ACS Nano 5 (2011) 4350.

[35] C. Ranaveeraa, Z. Wanga, E. Alqurashia, B.K. Guptab, R.K. Gupta*A, J. Mater. Chem. A 4 (2016) 9014.

[36] S.Y. Ji, T.T. Li, Z. Gao, Y.Y. Song, J.J. Xu, Chem. Commun. 54 (2018) 8765.

[37] Y.H. Deng, C. Ye, B.X. Tao, G. Chen, Q. Zhang, H.Q. Luo, N.B. Li, J. Power Sources 397 (2018) 44.

[38] J.W. Zhong, T. Wu, Q. Wu, S. Du, D.C. Chen, B. Chen, M.L. Chang, X.H. Luo, Y. L. Liu, J. Power Sources 417 (2019) 90.

[39] E. Fabbri, T.J. Schmidt, ACS Catal. 8 (2018) 9765.

[40] Z. Xiao, G. Xiao, M. Shi, Y. Zhu, ACS Appl. Mater. Interfaces 10 (2018) 16436.

[41] Z. Li, W. Feng, Y. Lin, L. Xin, H. Fei, RSC Adv. 6 (2016) 70632.

[42] S.H. Guo, W.Q. Chen, M. Li, J. Wang, F. Liu, J.P. Cheng, Electrochim. Acta 271 (2018) 498.

[43] W. Chen, C. Xia, H.N. Alshareef, ACS Nano 8 (2014) 9531.

[44] C. Guan, J. Liu, Y. Wang, L. Mao, Z. Fan, Z. Shen, H. Zhang, J. Wang, ACS Nano 9 (2015) 5198.